# Using secondary-proton spectra to study the compression and symmetry of deuterium-filled capsules at OMEGA

F. H. Séguin, C. K. Li, J. A. Frenje, D. G. Hicks,[a] K. M. Green, S. Kurebayashi, and R. D. Petrasso[b]
*Plasma Science and Fusion Center, Massachusetts Institute of Technology, Cambridge, Massachusetts 02139*

J. M. Soures, D. D. Meyerhofer,[c] V. Yu. Glebov, P. B. Radha, C. Stoeckl, S. Roberts, and C. Sorce
*Laboratory for Laser Energetics, University of Rochester, Rochester, New York 14623*

T. C. Sangster and M. D. Cable[d]
*Lawrence Livermore National Laboratory, Livermore, California 94550*

K. Fletcher and S. Padalino
*State University of New York, Geneseo, New York 14454*

(Received 18 July 2001; accepted 4 March 2002)

With new measurement techniques, high-resolution spectrometry of secondary fusion protons has been used to study compression and symmetry of imploded $D_2$-filled capsules in direct-drive inertial-confinement-fusion experiments at the 60-beam OMEGA laser facility [T. R. Boehly *et al.*, Opt. Commun. **133**, 495 (1997)]. Data from target capsules with ~15 atmospheres of $D_2$ fuel, in CH shells 19–27 $\mu$m thick, were acquired with a magnet-based, charged-particle spectrometer and with several new ''wedge-range-filter''-based spectrometers incorporating special filters and CR39 nuclear track detectors. Capsules with 19-$\mu$m shells, imploded with similar laser energies (~23 kJ) but different methods of single-beam laser smoothing, were studied and found to show different compression characteristics as indicated by the fuel areal density (determined by the ratio of secondary-proton yield to primary-neutron yield) and the total areal density (determined by the energy loss of protons due to slowing in the fuel and shell). In going from 0.3-THz SSD (smoothing by spectral dispersion) to 1-THz SSD and PS (polarization smoothing), the fuel areal density increased by at least 30%, while the total areal density increased by 40% (from ~52 to ~72 mg/cm$^2$). In addition, significant low-mode-number spatial asymmetries in implosions were indicated by spectra measured at different angles with respect to the target. The mean energies of protons, measured at different angles during the same shot, varied by as much as 1 MeV, implying angular variations in areal density of order 30 mg/cm$^2$. To the best of our knowledge, this is the first experimental demonstration that capsule symmetry can be sensitively studied by measuring the energy loss of charged particles. © *2002 American Institute of Physics.*
[DOI: 10.1063/1.1472502]

## I. INTRODUCTION

The potential utility of secondary fusion products for diagnosing implosions of $D_2$-filled capsules in inertial-confinement-fusion (ICF) experiments has been recognized for more than two decades,[1–8] but practical use of secondary-proton data has previously been limited by the lack of accurate spectroscopic measurement techniques. The implementation of two different types of charged-particle spectrometers has now made measurement and interpretation of high-resolution secondary-proton spectra possible. The measurement methods are described here, along with data and analysis having important implications for two physics issues that are crucial for the success of ICF. The first issue involves the impact of different methods of single-beam laser smoothing on implosion performance; the data presented here imply that better smoothing does result in better capsule compression, presumably due to a reduction in the seeding of high-mode-number Rayleigh–Taylor instabilities. The second issue involves low-mode-number asymmetries in the areal densities of imploded capsules; the data presented here provide the first experimental demonstration that such asymmetries can be studied by measuring the energy loss of charged particles due to slowing in the capsule plasma.

The general value of charged-particle spectrometry for capsule diagnostics has recently been demonstrated with magnet-based charged-particle spectrometers (CPSs), which are now used on a regular basis for measuring spectra of primary charged fusion products (p, D, T, $\alpha$) and ''knock-on'' particles (p, D, T, and $^3$He elastically scattered by 14.1-MeV neutrons[3])[9,10] for a wide range of capsule types and implosion conditions at the OMEGA 60-beam laser facility.[11] Measured spectra provide a number of important implosion

[a]Present address: Lawrence Livermore National Laboratory, Livermore, CA.
[b]Also visiting Senior Scientist, Laboratory for Laser Energetics, University of Rochester, Rochester, NY.
[c]Also at Departments of Mechanical Engineering and Physics, and Astronomy, University of Rochester, Rochester, NY.
[d]Present address: Xenogen Corporation, Alameda, CA.

 

parameters such as primary yields; fuel ion temperature; and areal density of fuel ($\rho R_{\text{fuel}}$), shell ($\rho R_{\text{shell}}$), or fuel plus shell ($\rho R_{\text{total}}$). Areal densities are determined by measuring the energy loss of charged fusion products as they pass out through fuel and shell,[9] or by measuring the yields of knock-on particles[10] or secondary fusion products.[1–8]

In the most important future ICF experiments utilizing cryogenic capsules with DT or $D_2$ fuel, large values of areal density will limit the number of diagnostic measurements that can be made of charged particles. On the National Ignition Facility (NIF), $\rho R_{\text{total}}$ of imploded DT capsules is eventually expected to exceed 1 g/cm$^2$. In this case, the only charged particles that could escape the fuel and be detected for studying $\rho R$ are tertiary protons,[12] which have energies as high as 30.8 MeV. DT capsules planned for OMEGA may (based on 1D simulations) reach $\rho R_{\text{total}}$ of 0.2 to 0.3 g/cm$^2$. In this case, knock-on deuterons and tritons, resulting from elastic collisions with primary 14.1-MeV neutrons, could be detected and used to study $\rho R$ with CPSs.[10]

In the shorter term, cryogenic experiments will be carried out with pure $D_2$ fuel. No primary charged fusion products will be energetic enough to escape and be detected, and there will be no high-energy primary neutrons to generate energetic knock-on particles. In addition, the method of determining $\rho R_{\text{fuel}}$ through a measurement of secondary-neutron yields[6] will be problematic for values of $\rho R_{\text{fuel}}$ exceeding $\sim$0.1 g/cm$^2$. Secondary D$^3$He protons (12.6–17.5 MeV), however, will escape from D capsules with relatively high $\rho R$. These protons are created by the two sequential reactions

$$\mathrm{D}+\mathrm{D}\rightarrow n(2.45\ \mathrm{MeV})+{}^3\mathrm{He}(0.82\ \mathrm{MeV}), \tag{1}$$

and

$$^3\mathrm{He}(\leqslant 0.82\ \mathrm{MeV})+\mathrm{D} \rightarrow \alpha(6.6-1.7\ \mathrm{MeV})+p(12.6-17.5\ \mathrm{MeV}). \tag{2}$$

In reaction (1), $^3$He is created with 0.82 MeV of kinetic energy. Some of the $^3$He ions then react in-flight with thermal D ions, creating protons which, because of the kinetic energy of the $^3$He, have a range of energies. Measured spectra of these protons can be used to study $\rho R_{\text{fuel}}$, $\rho R_{\text{total}}$, capsule symmetry, and sometimes other parameters.

The remainder of this paper will discuss the use of spectral measurements. Although the emphasis throughout is on secondary protons, there is also discussion of how they relate to secondary neutrons created by the two sequential reactions

$$\mathrm{D}+\mathrm{D}\rightarrow p(3.02\ \mathrm{MeV})+\mathrm{T}(1.01\ \mathrm{MeV}), \tag{3}$$

and

$$\mathrm{T}(\leqslant 1.01\ \mathrm{MeV})+\mathrm{D} \rightarrow \alpha(6.7-1.4\ \mathrm{MeV})+n(11.9-17.2\ \mathrm{MeV}). \tag{4}$$

Section II shows how the characteristics of secondary protons and neutrons are related to the physical parameters of capsules. Section III describes how proton spectra are measured with magnet-based charged-particle spectrometers (CPSs) and with ''wedge-range-filter''-based spectrometers (WRFs) that have recently been developed. Section IV describes specific experiments at OMEGA and secondary-proton data, while physical capsule parameters are derived from the data in Sec. V. The physics implications of these measured parameters are discussed in Secs. VI and VII.

## II. SECONDARY SPECTRA AND CAPSULE CHARACTERISTICS

Two simple models of plasma structure are used here to illustrate how measurements of secondary yields and spectra are related to the properties of compressed capsules.[7] In the ''hot-spot'' model, all primary fusion reactions take place in a small region at the center of the spherical fuel, and the fuel outside the hot spot, where the primary fusion products react with cooler fuel to create secondaries, has uniform density and temperature. In the ''uniform'' model, the fuel is uniform over its entire spherical volume so that primary and secondary reactions take place everywhere. In both cases, there can be a spherical shell or pusher of a different material outside the fuel (generally CH, in most current OMEGA experiments).

Modeling of the slowing down of primary $^3$He and T in D fuel can be carried out with the formalism described in Ref. 13, from which the stopping powers shown in Fig. 1 were calculated. The production rates for secondaries are then determined by the cross sections shown in Fig. 2, calculated from the formalism of Ref. 14. The resultant yields are described in Sec. II A, below. The shapes of the spectra of secondary protons and neutrons, as they are created in the fuel, are discussed in Sec. II B. Modifications to the spectrum of protons as they slow down on their way out of the fuel and shell are then determined by the stopping power illustrated in Fig. 3 (calculated according to Ref. 13) and described in Sec. II C.

### A. Yields

The yields of secondary protons and neutrons ($Y_{2\text{p}}$ and $Y_{2\text{n}}$) can be calculated by integrating over the appropriate paths of primary fusion products $^3$He and T, using the assumptions described above to calculate their energies as a function of position and the secondary production rates. The results are proportional to the primary-neutron yield $Y_{1\text{n}}$, as shown in Fig. 4. Related calculations were carried out for some of these cases by previous workers,[1–8] utilizing other models for the slowing down of $^3$He and T. They pointed out that as long as $\rho R_{\text{fuel}}$ is smaller than the range of one of the primary particles ($^3$He or T) in the fuel, there is a nearly linear relationship between $\rho R_{\text{fuel}}$ and the associated secondary-particle yield ratio ($Y_{2\text{p}}/Y_{1\text{n}}$ or $Y_{2\text{n}}/Y_{1\text{n}}$). When $\rho R_{\text{fuel}}$ exceeds the range of a given primary particle, the associated secondary-particle yield ratio reaches a saturation level, as shown in Fig. 4. For small enough $\rho R_{\text{fuel}}$, therefore, measurements of yield can be used to infer $\rho R_{\text{fuel}}$. The results depend weakly on plasma density, but the plasma temperature has a strong impact on the value of $\rho R_{\text{fuel}}$ at which the linear relationship fails due to complete slowing down of the primary particles in the fuel. This is a consequence of the temperature dependences of the total particle ranges, as illustrated in Fig. 5. Because of the cross sections of Fig. 2,

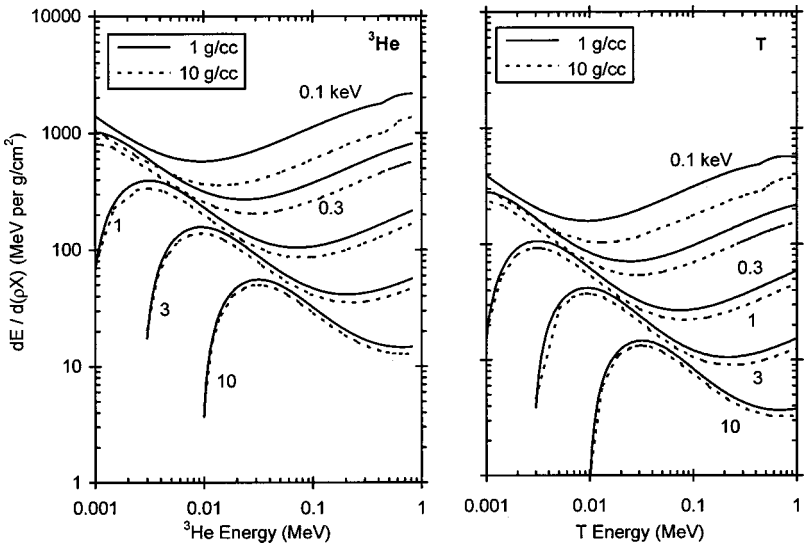


FIG. 1. Stopping powers for $^3$He (left) and T (right) in D plasmas with various electron temperatures (calculated according to Ref. 13). The stopping is dominated by electron-induced slowing at particle energies above about 100 times the electron temperature, and by ion-induced slowing at lower energies.

secondary protons are preferentially produced close to the birth position of primary $^3$He, while secondary neutrons are preferentially created near the end of the range of primary T (see Fig. 6).

Two differences between the hot-spot and uniform models are apparent in Fig. 4. The first is that the value of $\rho R_{\text{fuel}}$ for a given yield is higher in the uniform model, reflecting the fact that the mean distance traveled by primary particles before they encounter the fuel–shell interface is smaller by a factor of 0.75. The second difference is that complete saturation of yield at high values of $\rho R_{\text{fuel}}$ in the uniform model is approached asymptotically, but never reached, because some primaries are always created close enough to the surface to escape the fuel.

Although a measured secondary-proton yield can be used in the context of our models to infer $\rho R_{\text{fuel}}$ only in regimes where the primary $^3$He escape the fuel before stopping, other information can be inferred when complete stopping occurs in the fuel. As seen in Fig. 4, the electron temperature determines the maximum possible secondary-to-primary ratio $Y_{2\text{p}}/Y_{1\text{n}}$. If it is known that yield saturation has been reached, it is possible to estimate the effective electron temperature as illustrated in Fig. 7 (a similar relationship between electron temperature and yield saturation holds for secondary neutrons). If it is not known whether saturation has been reached, the measured secondary-to-primary ratio provides a minimum value for electron temperature.

It was assumed in this simple model that the capsule is spherically symmetric and there is no mixing of fuel and shell material. It will be shown in Sec. V C that deviations from spherical symmetry can occur, but when small they probably have relatively little effect on the ratios of total yields of different particles. Other work currently underway indicates that fuel–shell mixing may have significant effects on yields;[15] some of those effects will be taken into account in Sec. V A, when experimentally measured yields are interpreted.

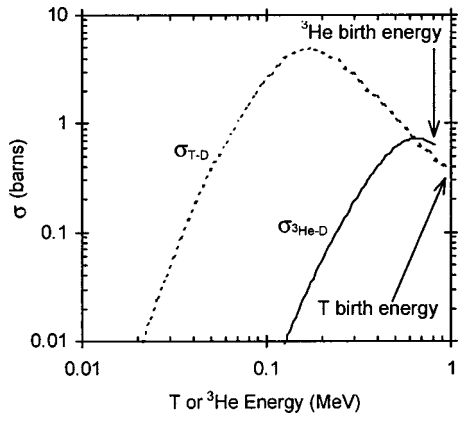


FIG. 2. Fusion cross sections for energetic $^3$He or T with cold D plasma (calculated according to Ref. 14).

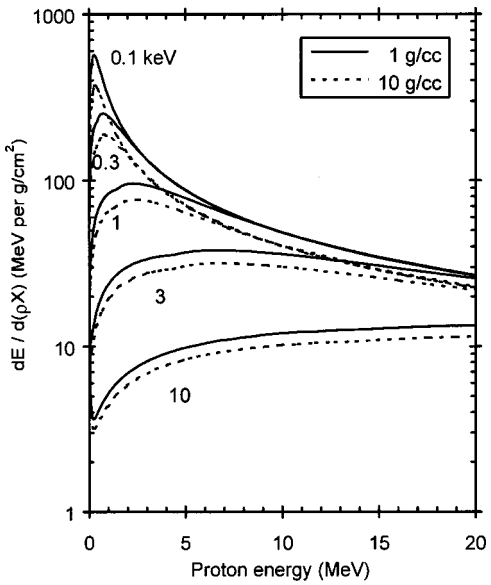


FIG. 3. Stopping power for protons in D plasmas with various electron temperatures (calculated according to Ref. 13). Over most of the energy range, where slowing is dominated by plasma electrons, the stopping power for CH plasmas is almost identical except for being higher by a factor of about 14/13 (the ratio of the numbers of electrons per unit mass).

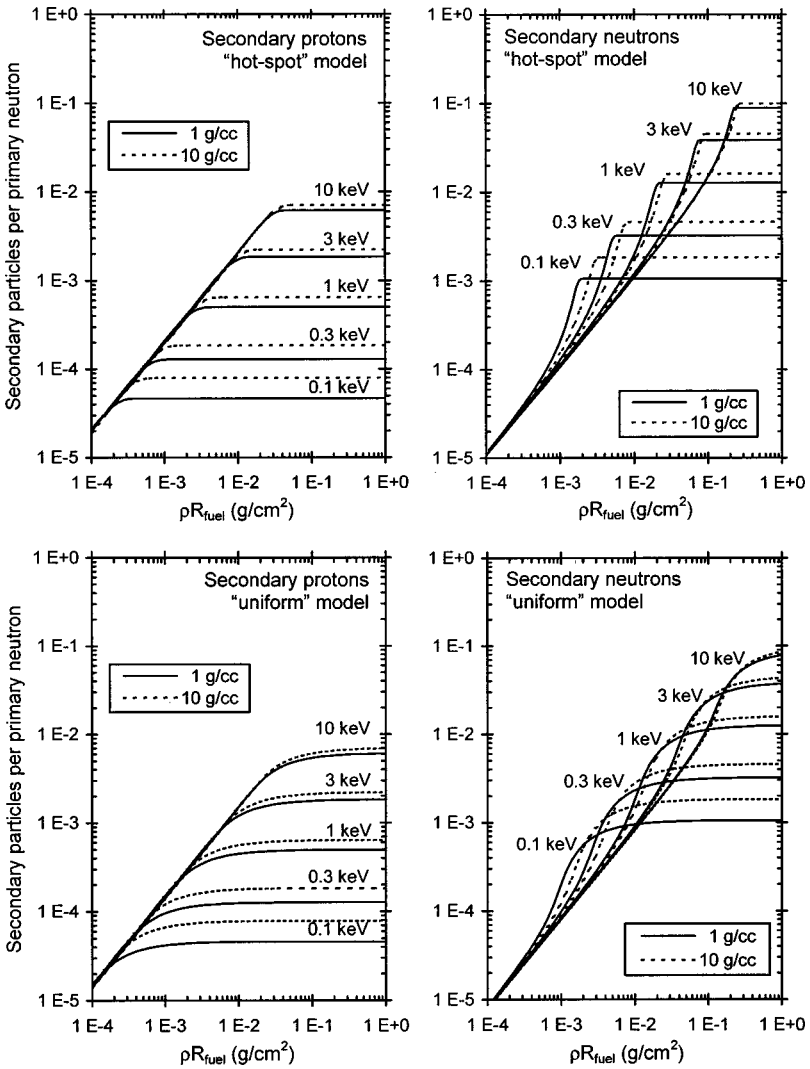


FIG. 4. Yields of secondary protons (left) and neutrons (right), calculated using Ref. 13 to model the slowing down of primary fusion products in a D plasma. The reaction cross sections of Fig. 1 were used, ignoring effects of thermal velocities of the D ions (which would be needed for ion temperatures above ~10 keV). The two top plots assume the "hot-spot" model, in which primary reactions all take place in a small region at the center, and secondary reactions take place outside the hot spot in a cooler fuel region which is uniform in density and temperature. The two bottom plots assume the "uniform" model in which primary and secondary reactions take place throughout the fuel plasma, which is uniform in temperature and density.

### B. Birth spectra

The shapes of the spectra of secondary particles at their birth can be calculated, and we begin with the secondary protons. If $\rho R_{\text{fuel}}$ is small, so that the primary $^3$He escape the fuel before losing much of their 0.82-MeV birth energy, then the protons they produce by fusing with fuel deuterons are equally distributed between limiting energies of about 12.6 and 17.5 MeV. The energy limits are defined by kinematics,

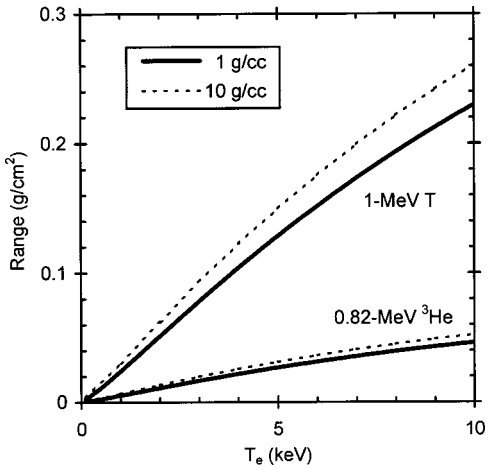


FIG. 5. Ranges of primary DD fusion products in a D plasma for different plasma densities and electron temperatures (from the stopping-power curves in Fig. 1).

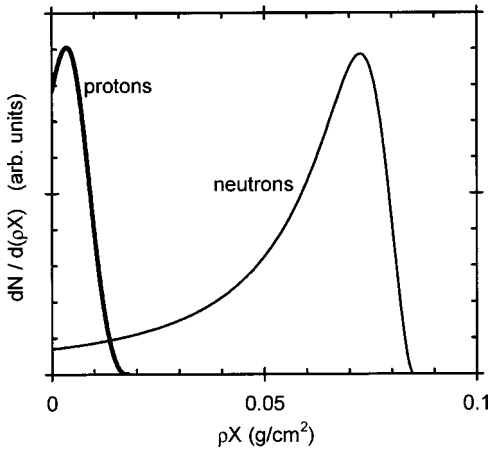


FIG. 6. Illustration of how secondary protons are mostly created near the birth position of the primary $^3$He, while secondary neutrons are mostly created toward the end of the range of primary T. The vertical axis is in arbitrary units that are different for the two curves; the horizontal axis unit $\rho X$ is the distance from primary birth position in g/cm$^2$ for a 3-keV, 3-g/cc D plasma.

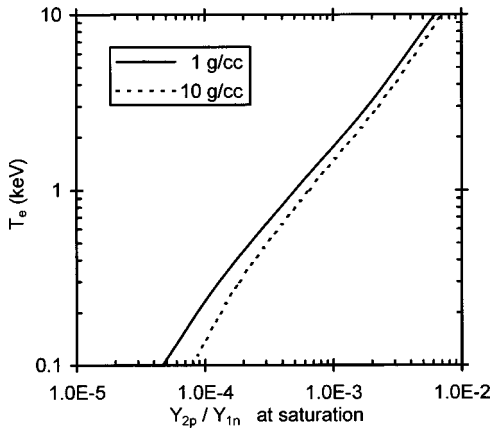


FIG. 7. Electron temperature for which $Y_{2p}/Y_{1n}$ cannot exceed a given saturation value (see Fig. 4; these numbers apply to both the hot-spot and uniform models). Under some circumstances, this relationship can be used to estimate $T_e$.

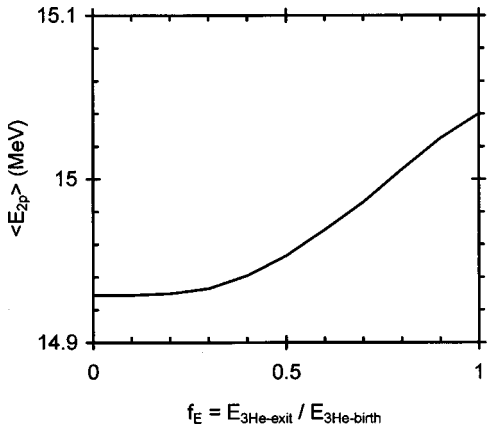


FIG. 9. Dependence of the mean energies of the proton birth spectra shown in the previous figure on the fraction of $^3$He energy remaining when the $^3$He reaches the fuel–shell interface. Plasma temperature was assumed to be 3 keV, and the density was 3 g/cc. $f_E$ is defined in the caption of Fig. 8. If the appropriate value of $f_E$ is not known, there will be a small uncertainty in the effective mean energy. In such a case, we could use the value 14.97 $\pm$0.04 MeV, which corresponds to the assumption of equal probability for all values of $f_E$.

and are determined by $^3$He energy at the time of interaction with D. The flat distribution as a function of energy between the limits can be demonstrated by assuming that fusion products are distributed isotropically in the $^3$He–D center-of-mass frame, transforming to the lab frame, and calculating the number of particles per unit energy. The number of protons $dN_{2p}$ produced during the slowing down of $N_{^3He}$ $^3$He from energy $E_{^3He}$ to $E_{^3He}-dE_{^3He}$ is

$$dN_{2p}/dE_{^3He}=AN_{^3He}\sigma_{^3He-D}(E_{^3He})/[dE_{^3He}/d(\rho X)],$$

where $\sigma_{^3He-D}(E_{^3He})$ is shown in Fig. 2, $X$ is distance along the trajectory of $^3$He in the plasma, $dE_{^3He}/d(\rho X)$ is shown in Fig. 1, and $A$ is a constant. For larger values of $\rho R_{fuel}$, some of the $^3$He will slow down before leaving the fuel; when they interact with the fuel, the kinematically defined width of the resultant proton spectrum will be smaller. Since $\sigma_{^3He-D}(E_{^3He})$ decreases rapidly as $E_{^3He}$ decreases below about 0.5 MeV, the contributions to the final proton spectrum become very small for lower-energy $^3$He and the shape of the total proton spectrum remains relatively insensitive to the amount of slowing down, or equivalently, the value of $\rho R_{fuel}$. This is demonstrated in Fig. 8(a), which shows how, in the case of a hot-spot model, the shape of the spectrum gets built up as a contribution of parts due to $^3$He slowed down by different amounts. Figure 8(a) also illustrates that the shape of the birth spectrum is relatively insensitive to the plasma temperature. The mean energy of the spectrum varies only slightly with the amount of slowing down of $^3$He, as shown in Fig. 9.

The secondary-neutron birth spectrum shape is more sensitive to $\rho R_{fuel}$ because the reaction cross section of the primary T with the fuel D increases rapidly as the T energy decreases (down to about $E_T=0.2$ MeV, as shown in Fig. 2). As discussed in previous work,[6–8] this means that the neutron spectrum gets narrower as $\rho R_{fuel}$ increases (and the exiting T energy decreases). Figure 8(b) illustrates this for the case of the hot-spot model.

### C. Measured spectra

A proton birth spectrum is never measured directly, because it is modified by passage through fuel and shell before the protons reach a spectrometer. Since the birth spectrum is relatively insensitive to fuel conditions, a measured spectrum contains diagnostic information about fuel and shell.

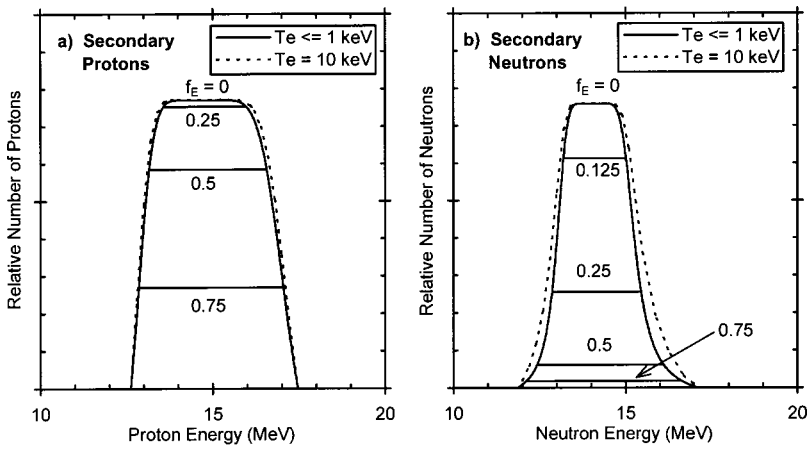


FIG. 8. Calculated shapes of secondary-proton and secondary-neutron spectra. These curves were generated by assuming that (i) the slowing of T or $^3$He in a D plasma varies with energy as shown in Fig. 1, and (ii) the primary particles are created near the center and pass through a uniform fuel that ranges their energies down to some fraction $f_E$ of their birth energy (hot-spot model). The plasma density was assumed to be 3 g/cc. On each plot, the different curves show how the spectrum shape is built up as the primary particle gets ranged down; the curves *do not* show how the *number* of secondary particles varies with $\rho R$. Each plot has one curve for plasma temperature 10 keV, corresponding to $f_E=0$. This curve is arbitrarily normalized so its amplitude is the same as the corresponding curve for lower temperature to demonstrate how the shape is not strongly dependent on temperature.

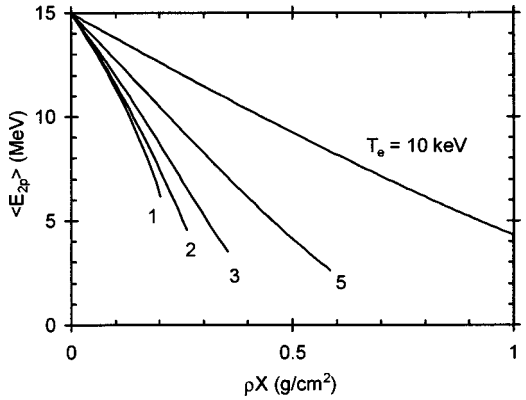


FIG. 10. The mean energy of a secondary-proton spectrum after slowing down in a D plasma with $\rho=3$ g/cc. The horizontal axis unit $\rho X$ is the distance from birth position in g/cm$^2$. For a CH plasma, the value of $\rho R$ corresponding to a given energy should be reduced by the factor 13/14 (the ratio of electrons per unit mass for D to the value for CH). The dependence on $\rho$ is weak; for $\rho R \leqslant 0.1$, the value of $\rho R$ corresponding to a given energy varies approximately as $\rho^{0.07}$.

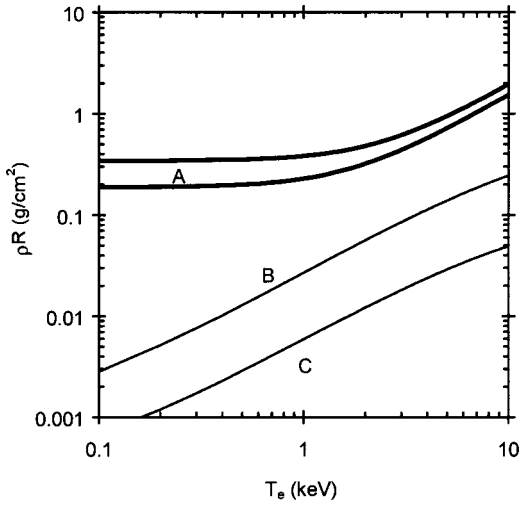


FIG. 11. Boundaries of regimes in which various measurements can give diagnostic information about a 3-g/cc, pure D plasma (assuming the hot-spot model; for the uniform model, results are similar). Note that $\rho R$ refers to $\rho R_{\text{total}}$ for curves A, but $\rho R_{\text{fuel}}$ for curves B and C. Measurements of secondary-proton energy shift and yield can be made only in the region *below* curve A, which show the total $\rho R_{\text{total}}$ at which secondary protons fail to escape from the plasma (one curve each for the upper and lower limits of the birth spectrum). Measurements of $Y_{2n}/Y_{1n}$ give information about $\rho R_{\text{fuel}}$ only in the region *below* curve B, which shows where primary T is ranged out completely by the fuel and the "saturated" regions of Fig. 4 are reached. *Above* curve B, measurement of $Y_{2n}$ could give information about the fuel electron temperature. Measurements of $Y_{2p}/Y_{1n}$ give information about $\rho R_{\text{fuel}}$ only in the region *below* curve C, which shows where primary $^3$He is ranged out completely by the fuel and the saturated regions of Fig. 4 are reached. *Above* curve C, measurement of $Y_{2p}$ can give information about the fuel electron temperature (see Fig. 7).

The mean energy of the secondary protons decreases according to the amount of material they traverse (Fig. 3 showed how the stopping power of fuel or shell plasma for protons varies with proton energy and plasma temperature). For the case of D and CH plasmas with $\rho=3$ g/cc, Fig. 10 illustrates the slowing down of secondary protons as a function of $T_e$ and $\rho X$, where $X$ is distance traveled through the plasma. The dependence on $\rho$ is weak; the ratio of $\rho X$ to the mean energy loss $\Delta\langle E_{2p}\rangle$ varies approximately as $\rho^{0.07}$ for $\rho X \leqslant 0.1$ g/cm$^2$. The dependence on temperature is weak for $T_e \leqslant 1$ keV and becomes progressively stronger for increasing $T_e$. If we assume that most of the protons are generated near the center of the fuel, then we can relate $\Delta\langle E_{2p}\rangle$ to a sum of the contributions from $\rho R_{\text{fuel}}$ and $\rho R_{\text{shell}}$. As we will see, $\rho R_{\text{shell}}$ is typically the dominant source of energy loss.

The protons are not all generated precisely at the center of the fuel, so they pass through slightly different amounts of material while leaving the capsule. This has an effect on the mean energy and on the spectrum width, but that effect is fairly small for the OMEGA data to be discussed here and will be ignored in estimating $\rho R_{\text{total}}=\rho R_{\text{fuel}}+\rho R_{\text{shell}}$ from the mean energy loss (see Ref. 16 for a quantitative discussion). The spectrum width can also be affected by time evolution.

More importantly, any long-wavelength variation of $\rho R_{\text{shell}}$ with position on the shell results in a different mean energy loss for protons detected at different angles with respect to the capsule, and any significant short-wavelength variation of $\rho R_{\text{shell}}$ could modify the width of an individual spectrum by causing different amounts of slowing down for different protons reaching the same detector. These effects will be discussed in Sec. VII.

A secondary-neutron birth spectrum can be measured directly,[17] because it is largely unaffected by passage out of the capsule. The shape of this spectrum is sometimes sensitive to fuel conditions, so it has potential diagnostic value.[8]

### D. Applicable plasma regimes

Figure 11 summarizes the plasma parameter regimes in which the measurement methods described above are applicable. Although the plotted boundaries of these regimes are based on simple models, they have more general applicability.

## III. INSTRUMENTS FOR MEASURING SECONDARY-PROTON SPECTRA

### A. Magnet-based charged-particle spectrometers

Two magnet-based spectrometers (CPS1 and CPS2) are installed on OMEGA (see Refs. 18, 19 and 16 for details). The principle of operation is illustrated in Fig. 12, which shows how a magnet is used to separate protons (and other charged particles) of different energies into different trajectories. The particles are stopped in CR39 nuclear track detectors, which are then etched in NaOH and scanned with a microscope. A small hole appears at the location of the track of each individual proton, and the position of a particle track gives the particle energy directly by virtue of the trajectory followed through the magnet. Final determination of the energy spectrum involves subtracting a background level due to neutron-induced noise and "intrinsic track noise." The neutron noise consists of tracks due to protons elastically scattered by primary fusion neutrons, either in the CR39 itself or in surrounding materials (approximately one noise event per

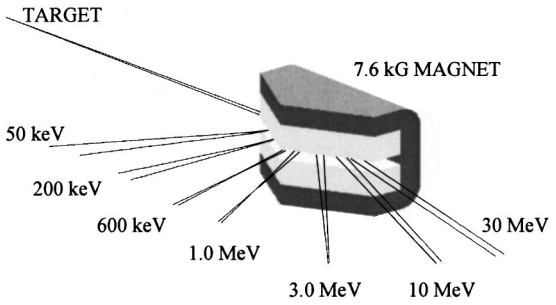


FIG. 12. Concept of the magnet-based charged-particle spectrometers (CPSs), showing how the magnetic field separates protons of different energies. Particles from the target capsule pass through a collimating aperture (not shown) before entering the magnet. After leaving the magnet, they are stopped in pieces of CR39 nuclear track detectors (not shown). The positions of the detected particles then indicate their energies by virtue of the trajectories followed.

$10^4$ neutrons[20]). The intrinsic track noise is due to structural defects in the CR39 that, after etching, are sometimes difficult to discriminate from particle tracks and generally appear at a density of at least 50 per $cm^2$.[16] Both types of noise tend to be uniformly distributed on the CR39, subject to counting statistics.

The absolute energy calibration of the CPSs is accurate to about $\pm 0.1$ MeV at 15 MeV.[21] The response function for a monoenergetic proton beam of a given energy is determined by the width of the entrance aperture; at 15 MeV, and with a 2-mm aperture, the response function is a square box with a half-width of 0.65 MeV (or a standard deviation of 0.38 MeV). Errors in yield measurements are limited by statistics, and the lowest value of $Y_{2p}$ for which CPS2 can measure a useful secondary-proton spectrum is roughly $10^8$ (constrained by the target-to-aperture distance of 100 cm, the entrance aperture size, the magnet dispersion, and the background noise level). CPS1 has a fixed target-to-aperture distance of about 235 cm, so it is less sensitive by about a factor of 5 and is generally not used to measure secondary-proton spectra.

### B. Wedge-range-filter spectrometers

A second type of spectrometer, a ''wedge-range-filter'' spectrometer (WRF), has recently been utilized for the first time. In a WRF (which will be described in greater detail elsewhere[16]), CR39 is again used as the particle detector, and a special wedge-shaped filter is used to range down the proton energies so they fall within the interval of sensitivity of the CR39 (approximately 0.5–7 MeV). This is a more complicated generalization of the simple range-filter (RF) measurements that have previously been made with fixed-thickness filters or step filters. Estimates of secondary-proton yields have previously been found with RFs by counting all proton tracks behind a constant-thickness filter,[3–6] and Azechi *et al.*[6] used such data to make broadband estimates of different parts of the proton spectrum. The disadvantages of the RF approach are that it is difficult to get accurate spectral information and that the interval of incident energies that can be detected with a single filter thickness is not wide enough to cover the entire secondary-proton spectrum.

In order to find an improved approach, we have performed highly detailed calibrations of the response of CR39 to protons of different energies (different energies result in different track sizes),[16] and calibrations of the transmission characteristics of various filters. In combination, those calibrations determine a direct mapping between track diameter and incident proton energy for a given filter thickness. That mapping can be used to reconstruct part of the incident spectrum from a histogram of track diameters, but for each filter thickness the incident energy interval that is most accurately reconstructed is less than 1 MeV wide. To accurately reconstruct the entire secondary-proton spectrum, which is at least 5 MeV wide, it is necessary to have data from many different filter thickness. For this reason a special ranging-filter design with continuously varying thickness was used, making possible the reconstruction of a continuous spectrum over a wide energy interval. The filters used here were machined from aluminum; each filter has thicknesses varying from 400 to 1800 $\mu$m. The individual filters are being calibrated absolutely[16] with protons with energies up to 13.8 MeV at the 2-MeV Van de Graaff accelerator at the SUNY Geneseo Nuclear Structure Laboratory, and current absolute-calibration uncertainties are $\pm 0.15$ MeV for energy and $\pm 12\%$ for yield measurement. The response for a monoenergetic, 13.8-MeV proton beam was determined to be roughly a Gaussian with a standard deviation of 0.15 MeV (approximately consistent with the amount of energy straggling expected for the protons as they pass through the filter).

The compactness, portability, and simplicity of WRFs makes it possible to deploy many of them on a single shot to study the spatial symmetry of proton spectra,[12,22,23] and also to get close to the target (12 cm) for high count rates and small statistical errors which allow measurement of good spectra for proton yields at least as low as the mid-$10^5$ range.

## IV. SPECTRUM MEASUREMENTS

### A. Experiments

Table I lists basic parameters for three sequences of implosions of $D_2$-filled capsules at OMEGA. In all cases, capsules with $\sim 15$ atm of $D_2$ fuel in CH shells were imploded by irradiation with about 22 kJ of 0.35-$\mu$m UV light applied in 60 beams with a 1-ns, square-top pulse. Sequences I and II, with 19-$\mu$m-thick capsule shells, were studied and contrasted to determine the difference in performance due to two methods of smoothing individual laser beams. In both cases the beams were smoothed by spectral dispersion (2D-SSD), but sequence I used three color cycles and 0.3-THz bandwidth,[24] while sequence II used one color cycle with 1-THz bandwidth plus polarization smoothing (PS)[25] using birefringent wedges with the laser, resulting in better single-beam uniformity. Sequence III was similar to sequence II except for a substantially larger shell thickness (27 $\mu$m) and a slightly larger outer diameter (about 980 $\mu$m); it is described here as a good illustration of implosion asymmetry.

TABLE I. Comparison of OMEGA shot sequences. The upper section of the table contains shot parameters (all shots utilized 1-ns square-top laser pulses), the middle section contains neutron and proton measurements, and the bottom section contains inferred capsule characteristics. All parameters represent averages over the shots within a sequence, and the energies and yields of secondary protons are also averaged over the measurements at different ports when appropriate. The values of $\rho R_{\text{fuel}}$ calculated from neutron yields are considered to be upper limits, as discussed in the text, while values calculated from proton yields are considered to be lower limits. Since we do not know what the radial profiles of temperature and density look like, the most conservative interpretation would use "hot-spot-model" proton numbers as lower limits and "uniform-model" neutron numbers as upper limits. Values of $\rho R_{\text{total}}$ are derived from the loss of energy of protons due to the fuel and shell, and represent the mean energy loss of the protons; if the spatial distribution of secondary-proton production extends to the inner boundary of the shell, then these numbers could include a slight overestimate of the true value of $\rho R_{\text{shell}}$, because the mean path through the shell will be longer than the radial path (see Ref. 16 for more discussion). See the text and the caption of Table II for discussion of measurement uncertainties. [p]From secondary-proton data. [n]From secondary-neutron data.

| Parameter | Sequence I (Shots 20 246,48,49,50) | Sequence II (Shots 20 689,90,91) | Sequence III (Shots 21 576,21 578) |
|---|---|---|---|
| Fuel | 14.3 atm $D_2$ | 15 atm $D_2$ | 15 atm $D_2$ |
| Shell | 19 $\mu$m CH | 19 $\mu$m CH | 27 $\mu$m CH |
| Diameter | 910 $\mu$m | 910 $\mu$m | 984 $\mu$m |
| Laser energy | 21.7 kJ | 23.2 kJ | 23.2 kJ |
| Laser smoothing | 0.3-THz SSD | 1-THz SSD+PS | 1-THz SSD+PS |
| $T_i$ (keV) | 3.3 | 3.7 | 2.4 |
| $Y_{1n}$ ($\times 10^{10}$) | 8.82 | 15.8 | 2.27 |
| $Y_{2n}$ ($\times 10^{7}$) | 13.1 | 38.0 | 5.04 |
| $Y_{2p}$ ($\times 10^{7}$) | 12.2 | 28.1 | 3.1 |
| $\langle E_{2p} \rangle$ (MeV) | 13.37 | 12.69 | 12.82 |
| $\rho R_{\text{fuel}}$ (mg/cm$^2$), "Uniform" model | $10^{p} \leqslant \rho R_{\text{fuel}} \leqslant 16^{n}$ | $14^{p} \leqslant \rho R_{\text{fuel}} \leqslant 24^{n}$ | $15^{p} \leqslant \rho R_{\text{fuel}} \leqslant 20^{n}$ |
| $\rho R_{\text{fuel}}$ (mg/cm$^2$), "hot-spot" model | $7^{p} \leqslant \rho R_{\text{fuel}} \leqslant 12^{n}$ | $9^{p} \leqslant \rho R_{\text{fuel}} \leqslant 19^{n}$ | $7^{p} \leqslant \rho R_{\text{fuel}} \leqslant 16^{n}$ |
| $\rho R_{\text{total}}$ (mg/cm$^2$) | $52^{p}$ | $72^{p}$ | $68^{p}$ |

### B. Data

Secondary-proton data for these sequences were recorded with a magnet-based spectrometer (CPS2) and with wedge-range-filter-based spectrometers. CPS2 data were acquired by exposing one piece of CR39 to the protons from all four shots of the first sequence, another piece to the protons from the three shots of the sequence II, and another to the protons from the two shots of sequence III, in order to sum the yields and minimize errors due to counting statistics for each sequence. Spectra for the first two sequences are shown in Fig. 13, but CPS2-measured results from sequence III are not shown because the total yield was too low to allow a statistically significant spectrum to be measured. WRF data were acquired for individual shots, with the spectrometers at a distance of 15 cm from the targets. Figure 14 shows spectra measured at three different positions during individual shots in sequences II and III. Figure 15 illustrates the spatial relationship between the target and the ports used for these measurements. Figures 16 and 17 show the measured yields and the energy shifts relative to the mean birth energy for all individual measurements in sequences II and III (where the total yield is inferred from the local fluence). The errors shown for WRF measurements reflect statistical errors and the calibration uncertainties discussed in Sec. III B. Mean values of the measured secondary-proton yields and energies are listed in Table I.

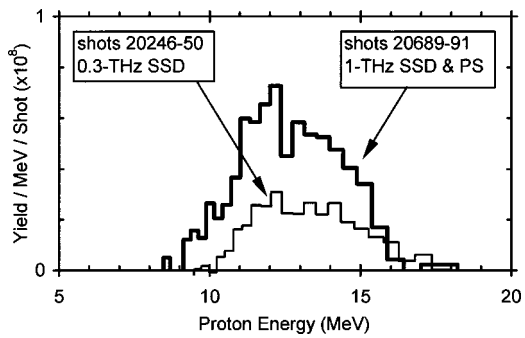


FIG. 13. Spectra of secondary protons for two shot series. Each spectrum represents an average over several nominally identical shots, measured with the magnet-based spectrometer CPS2.

Other measured parameters of the shots in the three sequences, measured with neutron diagnostics, are also listed in Table I. Primary-neutron yields $Y_{1n}$ were measured via indium activation, while ion temperatures were measured with a neutron time-of-flight diagnostic.[26] Secondary-neutron yields $Y_{2n}$ were measured with a time-of-flight diagnostic or with Cu activation.

## V. PHYSICAL INTERPRETATION OF MEASURED SPECTRA

The individual WRF-measured spectra for shots in sequences II and III show that measurements at different angles with respect to a target during the same shot sometimes differ. This is reflected in different mean energies and different inferred yields, as shown in Figs. 16 and 17, and in different widths, as shown in Fig. 18. These spatial variations in spectra put a fundamental limit on the accuracy of any

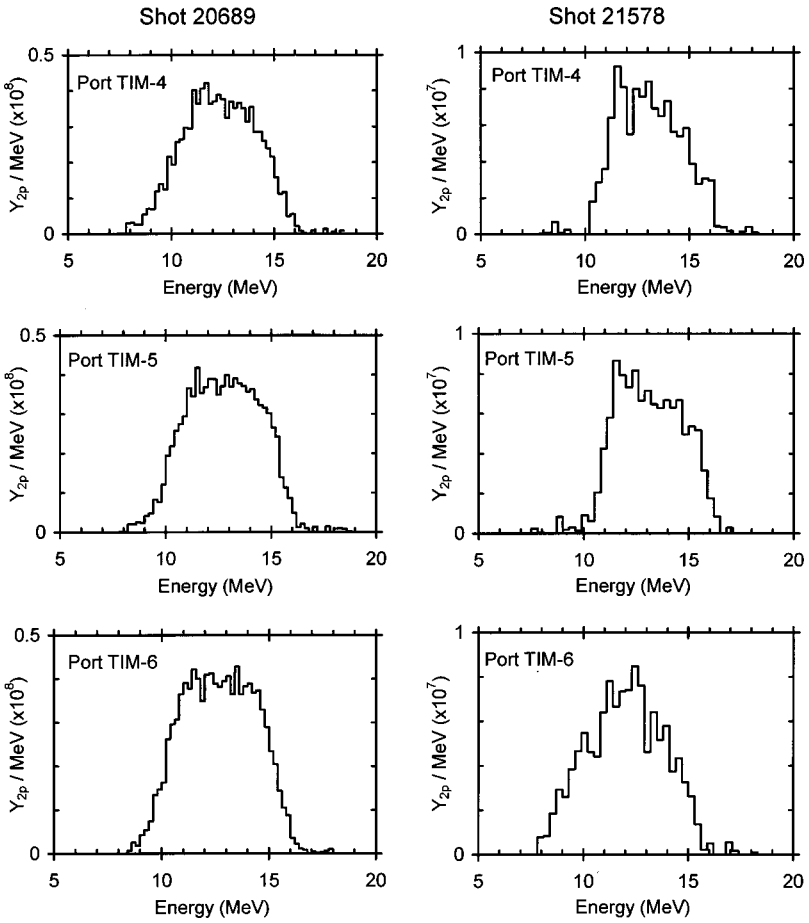


FIG. 14. Spectra of secondary protons for OMEGA shot 20 689, left, and OMEGA shot 21 578, right, as measured with wedge-range-filter spectrometers (WRFs). In each case, the OMEGA port is listed.

single spectral measurement as an indicator of overall capsule performance, and they complicate any effort to specify errors in deduced capsule parameters, but they contain important information about capsule asymmetries. As discussed in detail in Ref. 22, the energy asymmetries are interpreted as reflecting asymmetries in the capsule areal density, as predicted previously.[12] Yield asymmetries do not seem to be directly correlated with areal density asymmetries; there is evidence that they are at least partly due to very small modifications of particle trajectories outside the capsule that are not accompanied by measurable energy changes (perhaps by

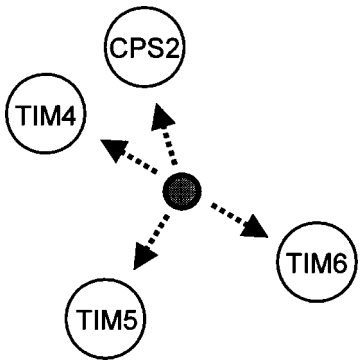


FIG. 15. Approximate relationship between the target (shown as the filled circle) and the OMEGA ports used in this study; they are roughly coplanar. The WRF spectrometers, on ports TIM4, TIM5, and TIM6, are approximately orthogonal to each other.

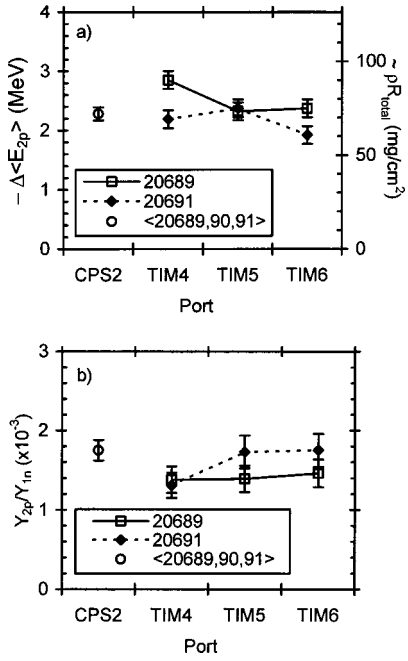


FIG. 16. Measured values of $\Delta\langle E_{2p}\rangle$ and $Y_{2p}/Y_{1n}$ for OMEGA shots 20 689, 20 690, and 20 691, some corresponding to spectra shown in Figs. 13 and 14. WRF measurements were not available for shot 20 690, and the CPS2 measurements correspond to averages over the three shots. The right-hand vertical axis of plot (a) is intended to indicate approximate values of $\rho R_{\text{total}}$ corresponding to individual shifts in mean proton energy. The error bars indicate measurement uncertainties for energy; uncertainties in inferred values of $\rho R_{\text{total}}$ would be somewhat larger to reflect uncertainties in other parameters used in the calculation of $\rho R_{\text{total}}$, as discussed in the text.

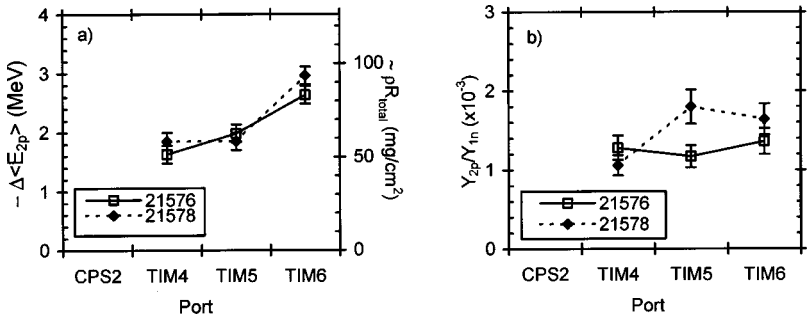


FIG. 17. WRF-measured values of $\Delta\langle E_{2p}\rangle$ and $Y_{2p}/Y_{1n}$ for OMEGA shots 21 576 and 21 578, some corresponding to the spectra shown in Fig. 14(b). No CPS2 data were available, because the yield was too low.

small magnetic fields). Accordingly, angular variations will be ignored below in discussions of yield except to the extent that they contribute to uncertainties in the total yield.

### A. Yields and fuel parameters

The ratio $Y_{2n}/Y_{1n}$ can be used to estimate $\rho R_{\text{fuel}}$ with the information in Fig. 4, subject to two caveats. First, preliminary numerical simulations suggest that any mixing at the shell–fuel interface may result in an increase in $Y_{2n}/Y_{1n}$ for a given $\rho R_{\text{fuel}}$. This is because the fuel edge temperature becomes lower, increasing the rate of slowing of the primary T (Fig. 1) and allowing them to reach energies where the cross section for secondary-neutron production is higher (Fig. 2) before leaving the fuel. Use of Fig. 4 with $Y_{2n}/Y_{1n}$, assuming an electron temperature equal to the neutron-averaged ion temperature, could therefore imply a value of $\rho R_{\text{fuel}}$ that is too high; secondary-neutron-derived values of $\rho R_{\text{fuel}}$ with these assumptions will therefore be interpreted as upper limits.[27] Second, the results are slightly dependent on assumptions we make about the density of the fuel. The mass density cannot be determined directly, but it turns out that the maximum possible value of $\rho R_{\text{fuel}}$ for these shots is about 25 mg/cm$^2$, and this information can be used with the capsule dimensions and fill pressure to estimate that $\rho$ is unlikely to exceed about 10 g/cc. Since inferred $\rho R_{\text{fuel}}$ increases very slowly with increasing $\rho$ here, use of this upper limit on $\rho$ is consistent with interpretation of inferred $\rho R_{\text{fuel}}$ as an upper limit (in any case, the results are extremely insensitive to the assumed value of $\rho$). These estimates of $T_e$ and $\rho$ are types of spatial averages, and radial profiles within the compressed core are unknown, making it difficult to determine directly whether the hot-spot or uniform model is more accurate. Both values are therefore listed in Table I for each shot sequence. The larger implied $\rho R_{\text{fuel}}$ of the uniform model can be chosen as a conservative upper limit, in which case the mean values for the three sequences are about 16, 24, and 20 mg/cm$^2$, respectively.

The measurements of $Y_{2p}/Y_{1n}$ can also be used in conjunction with Fig. 4 to study $\rho R_{\text{fuel}}$; results are listed in Table I. In this case there are reasons to interpret the results as lower limits. First, values of $Y_{2p}/Y_{1n}$ are very close to saturation in these experiments, especially if the electron temperature is assumed equal to the neutron-yield-weighted ion temperature. Second, preliminary work indicates that mixing at the shell–fuel interface may sometimes result in a small decrease in secondary-proton yield for a given $\rho R_{\text{fuel}}$, meaning that use of Fig. 4 could give us an inferred value of $\rho R_{\text{fuel}}$ that is too low. To be conservative, we could therefore choose the hot-spot values as extreme lower limits; the mean values for the three sequences are about 7, 9, and 7 mg/cm$^2$, respectively.

In Table I it can be seen that the proton-implied values of $\rho R_{\text{fuel}}$ are nearly always smaller than the neutron-implied values, although there tends to be slightly better agreement for the uniform model than for the hot-spot model. The discrepancy may be due to the effects of mixing, as discussed in Sec. V A. Alternatively, it could simply mean that the average electron temperature in the fuel is lower than the primary-yield-weighted ion temperature (as in the hot-spot model). A lower assumed average $T_e$ would sometimes lead to a larger proton-implied value for $\rho R_{\text{fuel}}$ and would always lead to a smaller neutron-implied value.

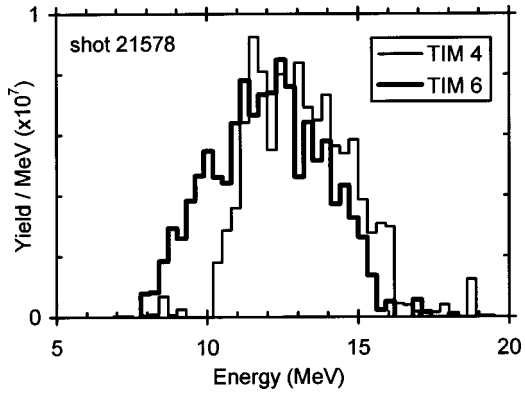


FIG. 18. Direct comparison of two WRF-measured spectra from shot 21 578.

### B. Energy shift and $\rho R_{\text{total}}$

The energy shift of a measured spectrum, relative to the birth spectrum, is due to proton slowing in both D fuel and CH shell. Figure 3 shows that the proton stopping powers normalized to $\rho$ are almost the same for D and for CH, and in the vicinity of the birth energies of the protons there is little variation with plasma temperature for $T_e < 3$ keV. In addition, it will turn out that the shell $\rho R$ dominates the total $\rho R$, and that the amount of slowing down in the fuel is small. We therefore estimate $\rho R_{\text{total}}$ from the shift in mean energy by using the relationship for CH described in Fig. 10 and its caption. The result is weakly dependent on electron temperature, and we assume that $T_e = (1 \pm 0.5)$ keV in the shell. There is also a very weak dependence on density, and we

assume that $\rho_{shell}=(20\pm10)$ gm/cc based on what has been inferred previously about shell compression.[17] These assumptions, together with the assumptions behind Fig. 10, lead to the inferred values of $\rho R_{total}$ shown in Table I if we use the average of the proton energies measured for each shot sequence. The uncertainties in inferred $\rho R_{total}$ due to the quoted uncertainties in temperature and density are typically $\leqslant 6\%$, but no uncertainties are listed in Table I because of the energy asymmetries discussed below.

Based on the assumption that measured asymmetries in proton energy during an individual shot represent areal density asymmetries, as discussed above, the right-hand vertical axes of Figs. 16(a) and 17(a) are labeled with $\rho R_{total}$ values appropriate for the directions corresponding to individual ports. The variations seen between different positions substantially exceed measurement uncertainties for shot sequence III.

To justify this association between energy asymmetries and capsule structure asymmetries, we need to explain why the observed energy asymmetry cannot be a result of uneven modification of proton energies by electric fields outside the capsule. This is an important issue, because we know that charged particles from implosions involving thinner shells and bang times occurring during the laser pulse experience acceleration ($\sim$0.5 MeV) due to a radial electric field generated by the laser–shell interaction.[9,21] We also know that electric fields dissipate after the laser pulse and that acceleration disappears by the bang time of the type of implosion under study here (hundreds of ps after the pulse). This is demonstrated directly by measurements we have made[10] of knock-on protons from implosions of DT-filled capsules with shells, fill pressures, and laser conditions comparable to those under study here. The knock-on protons are from the CH shell, elastically scattered by 14.1-MeV DT neutrons from the fuel. Because some of the protons are scattered just at the outer surface of the shell and will not slow down due to interactions with the capsule, the high-energy limit of the proton spectrum is always at 14.1 MeV. When we measure this spectrum at a number of different angles during each of a number of individual shots, using WRFs, the high-energy limit is always 14.1 MeV to within statistical and calibration uncertainties.[10] This shows that there is no significant change in proton energy during passage from the capsule to the detectors due to electric fields or any other mechanism.

## VI. IMPLICATIONS FOR SINGLE-LASER-BEAM SMOOTHING METHODS

The principal motivation for comparing sequences I and II was to see if an increase in the uniformity of individual laser beams would have a beneficial impact on capsule performance by reducing the seeding of high-mode-number ($l>10$) Rayleigh–Taylor instabilities. The smoothing method of sequence I is known to result in 3% to 8% rms deviations from uniformity within single beams, while the method of sequence II results in $\sim$1% nonuniformity. There are of course other sources of perturbations that can seed Rayleigh–Taylor instabilities, including low-mode-number ($l<10$) variations in irradiation uniformity due to errors in balancing the energies and adjusting the overlaps of different beams, and errors in surface finish in the capsules, so the relative importance of single-beam uniformity must be determined experimentally. The measurement methods described here do not give direct information about capsule structure at high mode numbers, but they do provide information about capsule compression.

TABLE II. Comparison of the $D_2$ implosions of sequences I and II to similar DT implosions (DT data from Ref. 10). Values corresponding to the "uniform" model are used, since that was the only model invoked in Ref. 10. As discussed in Sec. V, uncertainties in inferred values of $\rho R_{total}$ are not tabulated because of the unknown effects of angular variations. Uncertainties in $\rho R_{fuel}$ were not tabulated in Table I, because they are smaller than the differences between the proton-derived and neutron-derived values that were listed there as lower and upper limits; the uncertainties shown here reflect measurement uncertainties for all of the parameters used in the model calculations, plus statistical and calibration uncertainties in the measurements, plus an estimated uncertainty in yield due the angular variations seen during individual shots.

| | 0.3-THz SSD | | 1-THz SSD+PS | |
|---|---|---|---|---|
| | $\rho R_{fuel}$ (mg/cm$^2$) | $\rho R_{total}$ (mg/cm$^2$) | $\rho R_{fuel}$ (mg/cm$^2$) | $\rho R_{total}$ (mg/cm$^2$) |
| $D_2$ fuel (2n analysis) | $16\pm1$ | | $24\pm1$ | |
| $D_2$ fuel (2p analysis) | $10\pm2$ | 52 | $14+7-4$ | 72 |
| DT fuel (KO analysis) | $9\pm2$ | 56 | $15\pm3$ | 76 |

Table I shows that all tabulated parameters, measured and inferred, were better in sequence II than in sequence I. The yield-weighted ion temperature increased by 12%, the primary-neutron yield increased by 79%, and $\rho R_{total}$ increased by 38%. The inferred fuel areal density increased by 30%–60%, depending on whether the hot-spot or uniform model is used, and depending on whether the proton-derived value or the neutron-derived value is used. The radial compression ratio achieved during implosion can be inferred as $Cr=\sqrt{\rho R_{fuel}/\rho R_{fuel0}}$, where $\rho R_{fuel0}$ is the fuel areal density for the uncompressed capsule, and this parameter is higher by 13%–26% in sequence II than in sequence I.

These improvements all indicate that the lower single-beam nonuniformity of 1-THz SSD with PS, relative to 0.35-THz SSD without PS, leads to improvements in implosion performance for $D_2$-filled capsules of the type under study. It is of interest that the qualitative and quantitative improvement noted here is very similar to that which was seen in a parallel set of experiments with capsules that were filled with DT gas, where values of $\rho R_{fuel}$ and $\rho R_{total}$ were inferred by measuring yields of deuterons scattered from the fuel, and protons scattered from the shell, by primary 14.1-MeV DT neutrons.[10] The use of equivalent fill pressures, shells, and laser conditions should make the $D_2$-filled and DT-filled capsules hydrodynamically similar, and the numbers in Table II show that compression characteristics were very comparable. (The $D_2$ and DT data are used in a wider-ranging discussion of performance vs smoothing in Ref. 28.) The close correspondence of $\rho R_{fuel}$ values calculated from knock-on deuterons from DT capsules, which are independent of temperature and mix issues, and secondary protons from $D_2$ capsules, suggests that the secondary-proton-based values may be more accurate than the secondary-neutron-based values seen in the same table.

## VII. IMPLICATIONS FOR CAPSULE IMPLOSION SYMMETRY

Whereas high-mode-number structure cannot be seen directly with a small number of spectrometers separated by large angles, low-mode structure can.[22] The extremes in mean energy shown in Fig. 17 correspond to values of $\rho R_{\text{total}}$ of about 60 and 90 mg/cm$^2$ at different angles relative to the compressed capsules of both shots in sequence III. Each value should represent an average over a finite angular region of the shell, because the source of the secondary protons is likely to be distributed over a substantial fraction of the fuel volume (even in the hot-spot model). Variations in $\rho R_{\text{shell}}$ within the region sampled by a single spectral measurement would increase the spectrum width. The differences in width of the two spectra illustrated in Fig. 18 (for shot 21 578) probably reflect differing amounts of $\rho R$ variation within the regions sampled. The energy end points of a given spectrum can be used to estimate minimum and maximum integrated $\rho R$ for the detected protons, given that the minimum and maximum energies at birth are known to be 12.6 and 17.5 MeV. For the spectrum measured at port TIM-4, end points (after correction for the response function discussed in Sec. III B) imply minimum and maximum integrated $\rho R$ of approximately 50 and 62 mg/cm$^2$, respectively. For the spectrum measured at TIM-6, the extremes are about 80 and 110 mg/cm$^2$. Part of the difference between maximum and minimum integrated $\rho R$ within a single spectral measurement is due to path-length differences that would exist in a purely spherical model, as discussed in Sec. II C, but some of it in this case must be due to asymmetries.

Another characteristic of the energies plotted in Fig. 17 is the apparent correlation between the variations within shot 21 576 and those within shot 21 578. In both cases, the measurement at port TIM-6 gave a mean energy significantly lower than the measurements at TIM-4 or TIM-5. This may be related to observations reported from x-ray images of the cores of other imploded capsules, which often show deviation from spherical symmetry with similar spatial orientation for similar shots.[29] That asymmetry has been interpreted as due to systematic imbalances in laser power deposition on the capsule or to a slight error in positioning of the capsule.[30]

With only three spectra per shot, it is not possible to attempt a three-dimensional representation of the capsule structure or to perform any mode decomposition. Nevertheless, these measurements are important in indicating that strong asymmetries sometimes exist at burn time. We have recently observed similar (1 MeV or larger) differences in energy at different measurement positions for primary protons from some implosions of D$^3$He-filled capsules with 19-$\mu$m CH shells. These experiments were more comprehensive, involving nine different spectral measurements for each shot (using 7 WRF spectrometers and two CPSs). The variations will be described elsewhere, but they confirm the basic behavior observed here and provide more direct information about the relationship between laser beam balance and small-mode-number capsule asymmetries.[22]

## VIII. CONCLUSIONS

We have shown the first detailed measurements of secondary-proton spectra from $D_2$-filled capsules in ICF experiments, demonstrating the performance of two new diagnostic techniques and demonstrating that charged-particle spectrometry can provide useful diagnostic information about these capsules. Although more complicated modeling is now being developed for capsules with mix,[15,28] and for directly relating arbitrary capsule structures to the specific shapes and angular distributions of measured proton spectra, the simple methods used here have already been combined with the high-quality spectral measurements to provide information about two important physics issues. Studies with different single-beam laser smoothing techniques demonstrated that the compression of $D_2$-filled capsules is better with 1-THz SSD and PS than with 0.35-THz SSD without PS, and verified that the compression obtained with $D_2$ fuel is approximately the same as that obtained with DT fuel. In addition, the data here provide the first experimental demonstration that low-mode-number capsule $\rho R$ asymmetries can be studied by measuring the energy loss of charged particles due to slowing in the capsule plasma, as suggested in earlier work.[12] This result has already inspired a new range of symmetry experiments, using charged particles, for studying many types of capsules (including cryogenic $D_2$ capsules) and for studying the effects of laser beam balance.[22]

## ACKNOWLEDGMENTS

We thank Brock Bose for assistance in scanning CPS2 data for this paper.

The work described here was performed in part at the LLE National Laser Users' Facility (NLUF), and was supported in part by U.S. Department of Energy Contract No. DE-FG03-99SF21782, LLE subcontract number PO410025G, LLNL subcontract number B313975, and the U.S. Department of Energy Office of Inertial Confinement Fusion under Cooperative Agreement No. DE-FC03-92SF19460. Part of this work was also performed under the auspices of the U.S. Department of Energy by University of California Lawrence Livermore national Laboratory under Contract No. W-7405-Eng-48.

[1] H. D. Campbell and F. H. Southworth, in *Proceedings of the First Topical Meeting on the Technology of Controlled Nuclear Fusion* (American Nuclear Society, LaGrange Park, IL, 1974), p. 75.
[2] E. G. Gamalii, S. Yu, Gus'kov, O. N. Krokhin, and V. B. Rusanov, JETP Lett. **21**, 70 (1975).
[3] S. Skupsky and S. Kacenjar, J. Appl. Phys. **52**, 2608 (1981).
[4] T. E. Blue and D. B. Harris, Nucl. Sci. Eng. **77**, 463 (1981).
[5] T. E. Blue, J. W. Blue, J. S. Durham, D. B. Harris, A. S. Hnesh, and J. J. Reyes, J. Appl. Phys. **54**, 615 (1983).
[6] H. Azechi, N. Miyanaga, R. O. Stapf *et al.*, Appl. Phys. Lett. **49**, 555 (1986).
[7] H. Azechi, M. D. Cable, and R. O. Stapf, Laser Part. Beams **9**, 119 (1991).
[8] M. D. Cable and S. P. Hatchett, J. Appl. Phys. **62**, 2233 (1987).
[9] C. K. Li, D. G. Hicks, F. H. Séguin *et al.*, Phys. Plasmas **7**, 2578 (2000).
[10] C. K. Li, F. H. Séguin, D. G. Hicks *et al.*, Phys. Plasmas **8**, 4902 (2001).
[11] T. R. Boehly, D. L. Brown, R. S. Craxton *et al.*, Opt. Commun. **133**, 495 (1997).

[12]R. D. Petrasso, C. K. Li, M. D. Cable *et al.*, Phys. Rev. Lett. **77**, 2718 (1996).
[13]C. K. Li and R. D. Petrasso, Phys. Rev. Lett. **70**, 3059 (1993).
[14]S. Glasstone and R. H. Lovberg, *Controlled Thermonuclear Reactions: An Introduction to Theory and Experiment* (Van Nostrand, Princeton, NJ, 1960).
[15]P. B. Radha, V. Yu. Glebov, F. J. Marshall *et al.*, Bull. Am. Phys. Soc. **45**, 164 (2000).
[16]F. H. Séguin, J. A. Frenje, C. K. Li *et al.*, ''Spectrometry of charged particles from inertial-confinement-fusion plasmas,'' Rev. Sci. Instrum. (submitted).
[17]F. H. Marshall, J. A. Delettrez, R. Epstein *et al.*, Phys. Plasmas **7**, 2108 (2000).
[18]D. G. Hicks, Ph.D. thesis, Massachusetts Institute of Technology (1999).
[19]D. G. Hicks, C. K. Li, R. D. Petrasso, F. H. Séguin, B. E. Burke, J. P. Knauer, S. Cremer, R. L. Kremens, M. D. Cable, and T. W. Phillips, Rev. Sci. Instrum. **68**, 589 (1997).
[20]J. A. Frenje, C. K. Li, F. H. Séguin, D. G. Hicks, S. Kurebayashi, R. D. Petrasso, S. Roberts, V. Yu Glebov, D. D. Meyerhofer, J. M. Soures, C. Chiritescu, G. J. Schmid, T. C. Sangster, and R. A. Lerche, ''Absolute measurements of neutron yields from DD and DT implosions at the OMEGA laser facility using CR-39 track detectors,'' Rev. Sci. Instrum. (to be published).
[21]D. G. Hicks, C. K. Li, F. H. Séguin *et al.*, Phys. Plasmas **7**, 5106 (2000).
[22]F. H. Séguin, C. K. Li, J. A. Frenje *et al.*, ''Measurements of $\rho$R asymmetries at burn time in inertial-confinement-fusion capsules,'' Phys. Plasmas (submitted).
[23]P. B. Radha, J. A. Delettrez, R. Epstein *et al.*, Bull. Am. Phys. Soc. **44**, 194 (1999).
[24]S. Skupsky and R. S. Craxton, Phys. Plasmas **6**, 2157 (1999).
[25]T. R. Boehly, V. A. Smalyuk, D. D. Meyerhofer *et al.*, J. Appl. Phys. **85**, 3444 (1999).
[26]M. A. Russotto and R. L. Kremens, Rev. Sci. Instrum. **61**, 3125 (1990).
[27]It is possible to calculate a lower value of $\rho R_{\mathrm{fuel}}$ from the secondary-neutron yield by assuming that the mean electron temperature was equal not to the primary-yield-averaged ion temperature but to the value inferred from Fig. 7, with the assumption that the measured secondary-proton yield was in saturation. This implicitly assumes that the tritons producing secondary neutrons through reaction (4) saw the same mean electron temperature as the $^3$He that produced the secondary protons through reaction (2), which would be true if the fuel was uniform but not if the temperature profile was centrally peaked.
[28]D. D. Meyerhofer, J. A. Delettrez, R. Epstein *et al.*, Phys. Plasmas **8**, 2251 (2001).
[29]F. J. Marshall, J. A. Delettrez, D. D. Meyerhofer *et al.*, Bull. Am. Phys. Soc. **44**, 163 (2000).
[30]F. J. Marshall, private communication (2001).